Sulfate-Decorated Amorphous-Crystalline Cobalt-Iron Oxide Nanosheets to Enhance O-O Coupling in the Oxygen Evolution Reaction

Xiang Wang,*[a,b] Junshan Li,[c] Qian Xue,[d] Xu Han,[e] Congcong Xing,[b,f] Zhifu Liang,[b,e] Pablo Guardia,[b,g] Yong Zuo,[b,h] Ruifeng Du,[b] Lluis Balcells,[g] Jordi Arbiol,[e,i] Jordi Llorca,[f] Xueqiang Qi,*[b,d] Andreu Cabot*[b,i]

[a] School of Chemical Engineering and Pharmacy, Wuhan Institute of Technology, Wuhan 430205, China.

[b] Catalonia Institute for Energy Research (IREC), Sant Adrià de Besòs, 08930 Barcelona, Spain

[c] Institute of Advanced Study, Chengdu University, Chengdu 610106, China.

[d] School of Chemistry and Chemical Engineering, Chongqing University of Technology, Chongqing, 400054, China.

[e] Catalan Institute of Nanoscience and Nanotechnology (ICN2), Campus UAB, Bellaterra, 08193 Barcelona, Catalonia, Spain

[f] Institute of Energy Technologies, Department of Chemical Engineering and Barcelona Research Center in Multiscale Science and Engineering, Universitat Politècnica de Catalunya, EEBE, 08019, Barcelona, Catalonia, Spain

[g] Institut de Ciència de Materials de Barcelona, ICMAB-CSIC, Campus de la UAB, 08193 Bellaterra, Catalonia, Spain

[h] Istituto Italiano di Tecnologia, Via Morego 30, Genova, 16163 Italy

[i] ICREA Pg. Lluis Companys, 08010 Barcelona, Catalonia, Spain

* E-mail: xwang0612@gmail.com

* E-mail: xqqi@cqut.edu.cn

* E-mail: A. Cabot: acabot@irec.cat.

Abstract

The electrochemical oxygen evolution reaction (OER) plays a fundamental role in several energy technologies, which performance and cost-effectiveness are in large part related to the used OER electrocatalyst. Herein, we detail the synthesis of cobalt-Iron oxide nanosheets containing controlled amounts of well-anchored SO_4^{2-} anionic groups ($CoFe_xO_y$-SO_4). We use a cobalt-based zeolitic imidazolate framework (ZIF-67) as the structural template and cobalt source and Mohr's salt ($(NH_4)_2Fe(SO_4)_2{\cdot}6H_2O$) as the source of iron and sulfate. When combining the ZIF-67 with ammonium iron sulfate, the protons produced by the ammonium ion hydrolysis ($NH_4^+ + H_2O = NH_3{\cdot}H_2O + H^+$) etch the ZIF-67, dissociating its polyhedron structure, and form porous assemblies of two-dimensional nanostructures through a diffusion-controlled process. At the same time, iron ions partially replace cobalt within the structure, and SO_4^{2-} ions are anchored on the material surface by exchange with organic ligands. As a result, ultrathin $CoFe_xO_y$-SO_4 nanosheets are obtained. The proposed synthetic procedure enables controlling the amount of Fe and SO_4 ions and to analyze the effect of each element on the electrocatalytic activity. The optimized $CoFe_xO_y$-SO_4 material displays outstanding OER activity with a 10 mA cm^{-2} overpotential of 268 mV, a Tafel slope of 46.5 mV dec^{-1}, and excellent stability during 62 h. This excellent performance is correlated to the material's structural and chemical parameters. The assembled nanosheet structure is characterized by a large electrochemically active surface area, a high density of reaction sites, and fast electron transportation. Meanwhile, the introduction of iron increases the electrical conductivity of the catalysts and provides fast reaction sites with optimum bond energy and spin state for the adsorption of OER intermediates. The presence of sulfate ions at the catalyst surface modifies the electronic energy level of active sites, regulates the adsorption of intermediates to reduce the OER overpotential, and promotes the surface charge transfer, which accelerates the formation of oxygenated intermediates. Overall, the present work details the synthesis of a high-efficiency OER electrocatalyst and demonstrates the introduction of non-metallic anionic groups as an excellent strategy to promote electrocatalytic activity in energy conversion technologies.

Keywords: Sulfate, amorphous catalyst, cobalt-iron oxide, nanosheet, lattice oxygen oxidation, oxygen evolution reaction.

1. Introduction

The oxygen evolution reaction (OER) is the limiting step in various electrochemical energy technologies, such as water electrolysis, metal-air batteries, regenerative fuel cells, and electrochemical CO_2 reduction.[1-3] OER is characterized by high overpotentials and slow kinetics associated with the need to transfer four electrons to generate each O_2 molecule, the formation of multiple intermediates (*OH, *O, and *OOH) and the demanding O–O bond realization.[4-7] Owing to its high technological and socio-economic interest, numerous classes of materials have been tested as OER electrocatalysts. Amongst them, transition metal phosphides, nitrides, and chalcogenides have been recently reported as particularly active OER catalysts, reaching similar and even better performance than benchmark IrO_2 and RuO_2 electrocatalysts in alkaline electrolytes.[8-10] Nevertheless, in alkaline media, we and others have demonstrated the chemical conversion and restructuration of the surface of metal oxide, nitrides, phosphides, or chalcogenides (MX; X=O, N, P, S, Se) to form more active hydroxide (MOH) and mainly oxohydroxide (MOOH) that are found to be the true OER active species.[11-17] Thus the properties of the derived oxide, hydroxide, or oxohydroxide surfaces have been the focus of several recent studies. However, during this surface reconstruction, the surface anions are simultaneously oxidized to nitrates (NO_3^-), phosphates (PO_4^{3-}), sulfates (SO_4^{2-}), and selenates (SeO_4^{2-}),[18-20] which presence on the catalyst surface and role in the electrocatalytic reaction have been largely overlooked.

Few recent works have demonstrated the presence of nonmetallic anionic groups as key to boosting water oxidation activity.[21-25]. Accordingly, the engineering of oxides containing controlled amounts of these groups could be a promising strategy to improve the surface reaction kinetics.[25, 26] Nevertheless, the introduction of nonmetallic anionic groups through the indirect conversion of non-metallic elements leads to uncontrolled amounts of this impurity, which limits the optimization of the catalyst. On the other hand, the introduction of

anionic groups a posteriori, through surface adsorption, results in a weak chemical interaction that limits the effectiveness and stability of the resultant materials.[18, 21] Thus, an approach for the direct incorporation of controlled amounts of anionic groups that enable a strong bonding between anions and metal atoms is intensely pursued as it is expected to facilitate water oxidation.

On the other hand, some amorphous catalysts present improved OER performance over their crystalline counterpart.[27, 28] Amorphous catalysts are characterized by a large versatility in terms of atomic arrangement and composition, with easier assimilation of different types and concentrations of doping impurities.[29-31] Amorphous structures, having additional unsaturated coordination spheres also allow for the incorporation of multivalence metals with a wide range of oxidation states. Besides, compared with crystalline materials, amorphous oxides generally contain less strongly bond oxygen ions, which facilitates an efficient lattice oxygen-mediated OER mechanism.[32-36] As a drawback, the charge transfer kinetics of amorphous catalysts is limited by their lower electrical conductivity.[8, 37-39] Therefore, to rationally design and engineer optimized electrocatalysts, the balance between amorphous and crystalline phases is an additional key parameter to be tuned.

Herein, we introduce controlled amounts of SO_4^{2-} anionic groups into partially amorphous $CoFeO_x$ by a facile ion exchange and etching method. We thoroughly analyze the structural and chemical properties of the produced material and correlate them with their electrocatalytic performance. Exploiting the control possibilities provided by the synthesis method and taking into account the uncovered property-performance correlations, the electrocatalyst is optimized to reach outstanding OER performances.

2. Results and discussion

Figure 1 schematically displays the three-step process used to produce assembled $CoFe_xO_y$-SO_4 nanosheets. First, a crystalline cobalt-based zeolitic imidazolate framework (ZIF-67) was synthesized to be used as a structural template and cobalt source.[40, 41] Subsequently, ZIF-67 was reacted with $(NH_4)_2Fe(SO_4)_2{\cdot}6H_2O$ to etch the structure and partially exchange the metal (see the Experimental section for details). In this process, the protons produced by the

ammonium ion hydrolysis ($NH_4^+ + H_2O = NH_3 \cdot H_2O + H^+$) etch the ZIF-67, dissociating its polyhedron structure. We hypothesize that iron ions partially replace cobalt within the structure, and that using an iron sulfate salt, SO_4^{2-} ions are anchored on the material surface by exchange with organic ligands.

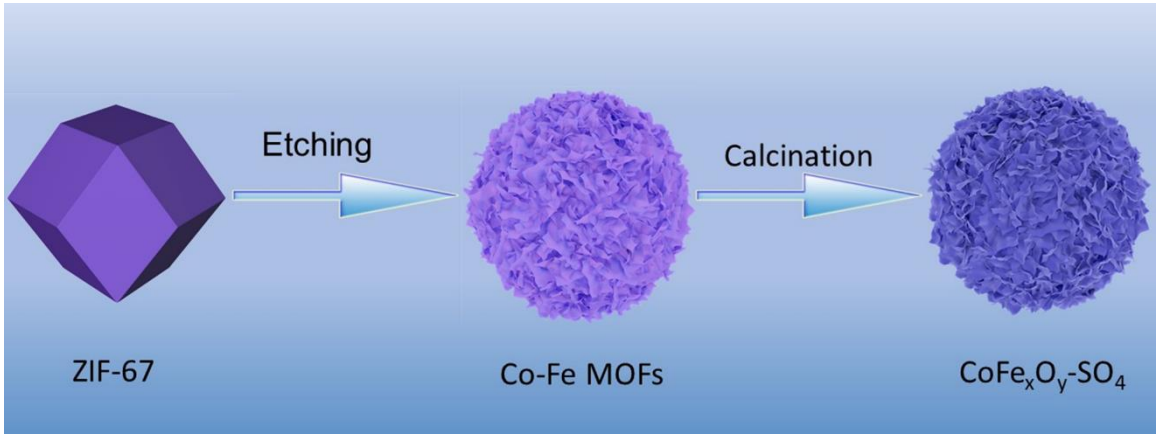

Figure 1. Schematic illustration of the $CoFe_xO_y$-SO_4synthesis process.

Figure 2a displays a representative SEM image of the ca. 350 nm ZIF-67 particles with rhombic dodecahedron geometry used as a template. XRD analysis showed the ZIF-67 template to be highly crystalline (Figure S1a). Upon reaction with the Mohr's salt, $(NH_4)_2Fe(SO_4)_2 \cdot 6H_2O$, a different structure progressively expands around the gradually disappearing ZIF-67 template (Figure 2b). Upon reacting for 12 h, the dodecahedral particle has been fully etched and only a porous nanosheet structure is observed (Figure S2). XRD analyses revealed the crystal structure of ZIF-67 to be lost after just 3 h of ion etching and exchange (Figures S1a and 3a).

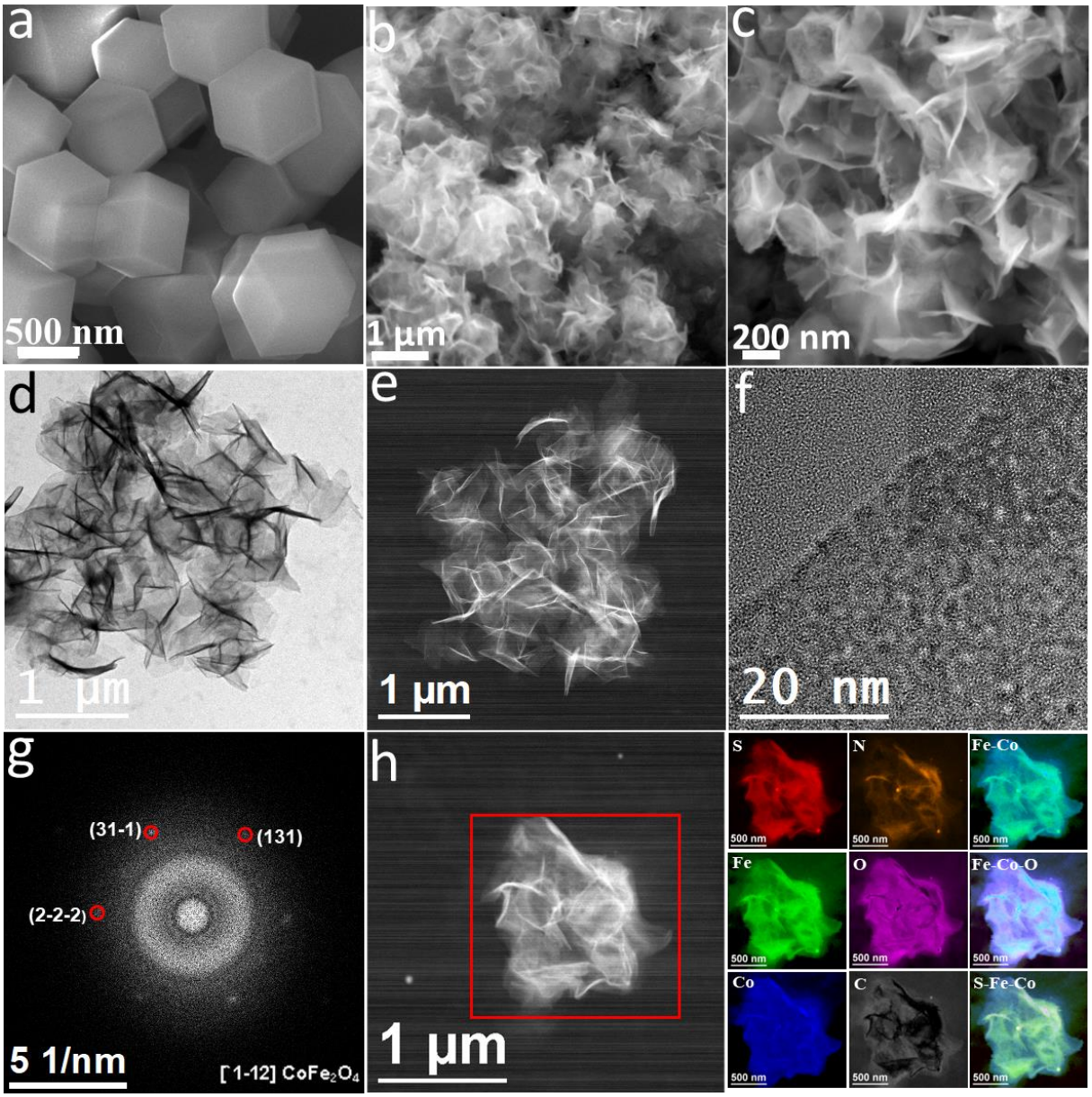

Figure 2. SEM images of a) ZIF-67, b) CoFe MOFs, and c) $CoFe_xO_y$-SO_4. d) TEM, e) HAADF image, f) HRTEM image, g) corresponding FFT spectrum, and h) EELS chemical composition maps of $CoFe_xO_y$-200 nanosheets. Individual S $L_{2,3}$-edges at 165 eV (red), Fe $L_{2,3}$-edges at 708 eV (green), Co $L_{2,3}$-edges at 779 eV (blue), N K-edge at 401 eV (orange), O K-edge at 532 eV (pink) and C K-edge at 284 eV (grey) and composites of Fe-Co, Fe-Co-O, and S-Fe-Co.

ZIF-67 and CoFe MOFs were annealed in air to remove organic ligands. The TGA curves displayed the main weight loss being completed at 280 °C for CoFe-MOFs and 350 °C for ZIF-67. Thus, 350°C was the selected temperature for annealing to minimize the material crystallization and carbon loss, which contributes to the charge transport while removing unstable organic ligands. Figure 2c-e, S3-11 shows SEM, TEM, and STEM images of the wrinkled nanosheets obtained after annealing the CoFe-MOF in an air atmosphere. HRTEM analysis

confirmed the amorphous structure of $CoFe_xO_y$ but detected some amorphous/crystalline interfaces (Figures 2f and S12). The fast Fourier transform (FFT) crystallographic analyses corroborated the presence of a small amount of weakly crystalline $CoFe_2O_4$ (Figure 2g). HAADF-STEM and EELS mapping (Figure 2h, S13) showed C, N, O, S, Co, and Fe to be distributed homogeneously within the nanosheets.

The material annealed at 350 °C presented an amorphous structure according to XRD patterns (Figure 3c). Only when increasing the annealing temperature to 450 °C and 550 °C, the mostly amorphous $CoFe_xO_y$ gradually transformed into crystalline $CoFe_2O_4$ (JCPDS card No. 01-1121, Figure 3c). Figures 3f and 3e display the Raman and FTIR spectra of the materials obtained from the annealing of ZIF-67 and CoFe-MOFs. Four peaks were detected in the Raman spectrum of the annealed ZIF-67, at 185.5, 465.3, 506.6, and 670 cm^{-1}, which were associated with the F^1_{2g}, E^2_g, F^2_{2g}, and A^1_g phonon modes of crystalline Co_3O_4.[42] With the introduction of iron sulfate, the Co_3O_4 phase peaks gradually weakened until disappearing. But a new peak of $CoFe_xO_y$-SO_4 at 350 cm^{-1} was formed, which could be ascribed to the Co–S coordination vibration.[43] On the other hand, all the materials produced using the iron sulfate salt displayed an evident FTIR absorption peak at about 1100 cm^{-1}, which is a fingerprint of the presence of SO_4^{2-} ions.

The average thickness of the $CoFe_xO_y$-SO_4 nanosheets was about 1.75 nm, as determined by AFM (Figure 3g). This 2D nanostructure dramatically increases the percentage of surface unsaturated atoms, provides a high electroactive surface area, and facilitates the rapid diffusion of reactant.[44, 45] From N_2 adsorption-desorption isotherms, the Brunauer-Emmett-Teller (BET) surface area of $CoFe_xO_y$-SO_4 was estimated at 133 $m^2\ g^{-1}$, over a fivefold above that of Co_3O_4 (26 $m^2\ g^{-1}$) obtained from the annealing of ZIF-67 (Figures 3h and S14). Besides, the Barrett-Joyner-Halenda (BJH) average pore size was 9 nm and 17 nm for $CoFe_xO_y$-SO_4 and Co_3O_4, respectively.

To demonstrate the key role played by Fe ions in the formation of the $CoFe_xO_y$-SO_4 nanosheets, ZIF-67 templates were reacted with $(NH_4)_2SO_4$. Without iron, the protons produced by ammonium ions cannot completely etch and dissociate the ZIF-67 (Figure S4). Thus, the polyhedron morphology and its crystal structure are largely preserved (Figure 3a). On the

other hand, to demonstrate the importance of selecting the proper salt, ZIF-67 was reacted with $FeCl_2$. In this case, ion etching and dissociation were too thorough, and most of the cobalt in the catalyst was lost, as observed by EDX analysis (Figure S5). After annealing in air at 350 °C, the products obtained from the reaction with $(NH)_2SO_4$ and $FeCl_2$ displayed a good crystal structure, assigned to Co_3O_4 (JCPDS card No. 42-1467) and α-Fe_2O_3 (JCPDS card No. 73-0603), respectively (Figure 3b).

The amount of Mohr's salt also controlled the final material architecture. A relatively large amount of $(NH_4)_2Fe(SO_4)_2$ was required to provide sufficient protons to fully etch the ZIF-67 template, while a low amount (100 mg) resulted in hollow polyhedral nanocages with few surface wrinkles (Figure S6, 3b). Besides, the amount of $(NH_4)_2Fe(SO_4)_2$ also controlled the iron content of the final material, which is a key parameter to optimizing its catalytic properties. In this direction, previous reports demonstrate the local spin state modification can strongly impact the material catalytic properties by further filling the e_g orbital as well as further overlapping the e_g orbital of the material with the adsorbed OH^-, thus promoting the creation of a Co-OH^- σ bond[18, 46, 47]. In our particular system, small amounts of $(NH_4)_2Fe(SO_4)_2$ (100 mg) resulted in highly Co-rich materials containing a very limited amount of iron. On the other hand, excess amounts of $(NH_4)_2Fe(SO_4)_2$ (400 mg) resulted in an almost full replacement of cobalt by iron ions (Figure S8). The change in the Fe content with the amount of $(NH_4)_2Fe(SO_4)_2$ salt used was also followed by characterizing the magnetic hysteresis loops of the samples. As displayed in Figures 4a and S15, the Curie temperature, magnetization, and coercive field increased with the amount of $(NH_4)_2Fe(SO_4)_2$ salt used, *i.e.* with the amount of Fe within the structure.

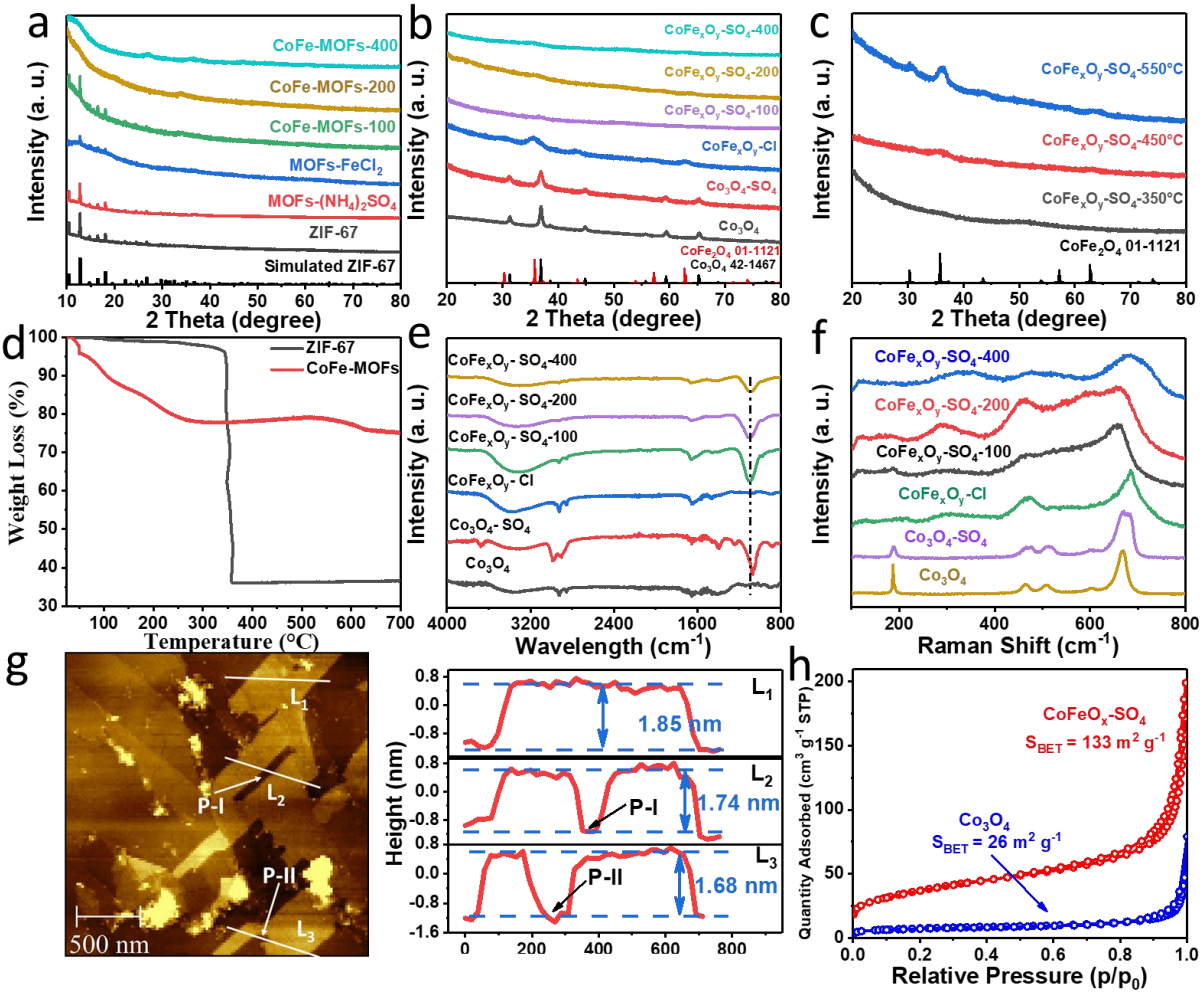

Figure 3. (a-c) XRD pattern of a) initial MOFs, b) Co_3O_4, Co_3O_4-SO_4, $CoFe_xO_y$-Cl, and $CoFe_xO_y$-SO_4 with different compositions, and c) $CoFe_xO_y$-200 after annealing at different temperatures. d) TGA curves from ZIF-67 and CoFe MOFs in air. e) FTIR spectra and f) Raman spectra of Co_3O_4, CoO_x-SO_4, $CoFe_xO_y$-Cl, and $CoFe_xO_y$-SO_4. g) AFM images and thickness of $CoFe_xO_y$-200. h) N_2 adsorption-desorption isotherms for $CoFe_xO_y$-200.

The bidentate-bond of SO_4^{2-} on the surface of $CoFe_xO_y$-SO_4 can introduce strongly acidic sites playing a role in the OER.[25] The existence of these acidic sites on $CoFe_xO_y$-SO_4 was evaluated using NH_3-TPD measurements, using the sulfate-free Co_3O_4 as a reference. As displayed in Figure 4b, Co_3O_4 shows weak NH_3-desorption peaks, which indicate a moderate density of intrinsic acidic sites on the Co_3O_4 surface. On the other hand, $CoFe_xO_y$-SO_4 shows strong NH_3-TPD peaks in the same temperature range, which indicates a high density of acidic sites associated with the presence of SO_4^{2-} on the $CoFe_xO_y$ surface.

The EPR spectrum of the catalyst was measured to explore species with unpaired electrons, and particularly oxygen vacancies that could generate high-energy dangling bonds at the

catalyst surface (Figure 4c).[48, 49] Using Co_3O_4 as a reference, we observed the signal at g = 2.12, associated with the presence of oxygen vacancies V_o, to be strongly enhanced in $CoFe_xO_y$-SO_4. This result demonstrates that the introduction of Fe and sulfate ions generate a large density of oxygen vacancies.

As shown in Figure S16, a clear XPS sulfur signal was detected from all catalysts produced from Mohr's salt. The S 2p XPS spectrum of the $CoFe_xO_y$-SO_4 catalyst exhibits a broad peak that can be fitted with two doublets with S $2p_{3/2}$ binding energies (BEs) at 168.8 eV (S $2p_{3/2}$) and 171.3 eV (S $2p_{3/2}$). The BE of the higher energy component coincides with that of sulfur within a sulfate chemical environment. This component increases with the amount of Fe and thus SO_4^{2-} introduced.[24, 50] Besides, the peaks at 160.2 and 162.2 eV were attributed to $2p_{3/2}$ and $2p_{1/2}$ of S ion within the lattice (S^{2-}).[43]

The O 1s XPS spectrum of $CoFe_xO_y$-SO_4 and Co_3O_4 (Figure 4d) displays 3 to 4 components. The component at lower BE is assigned to lattice oxygen, O_{Lat}. This component is located at 529 eV for Co_3O_4 and shifts to higher BEs with the incorporation of iron. The relative amount of this component detected at the material surface decreases with the amount of iron sulfate introduced. The component at an intermediate BE, at ca. 530-531 eV, is associated with oxygen-adsorbed species with lower oxygen coordination, O_{Ads}.[51, 52] A second component in the intermediate BE region, at ca. 532 eV, is associated with oxygen within sulfate ions O_{SO4}. This component significantly increases with the introduction of larger amounts of ammonium iron sulfate.[26] Finally, the component at higher BE, ca. 533-534 eV, is assigned to hydroxyl species and surface adsorbed water, O_{H2O}. This component also increases and shifts to higher BE with the introduction of Fe and sulfate.

The Co 2p XPS spectrum from all tested samples displays two chemical states, Co^{2+} and Co^{3+}, resembling that of Co within a Co_3O_4 lattice (Figure 4e).[53, 54] With the introduction of Fe and SO_4^{2-}, the peaks broaden and shift to higher BE, indicating an electronic interaction involving the transfer of charge between cobalt, iron and potentially SO_4^{2-} groups.[25, 26] Besides, the intensity of the Co XPS signal decreases with the introduction of Fe, consistently with the metal ion exchange and the results obtained from EDX analysis.

Figure 4e displays the Fe $2p_{3/2}$ XPS spectra. All spectra can be fitted with two components associated with Fe^{2+} and Fe^{3+} ions within an oxide lattice, although the component at higher BE, could be also assigned to Fe within a $FeSO_4$ chemical environment. [27, 36, 53]

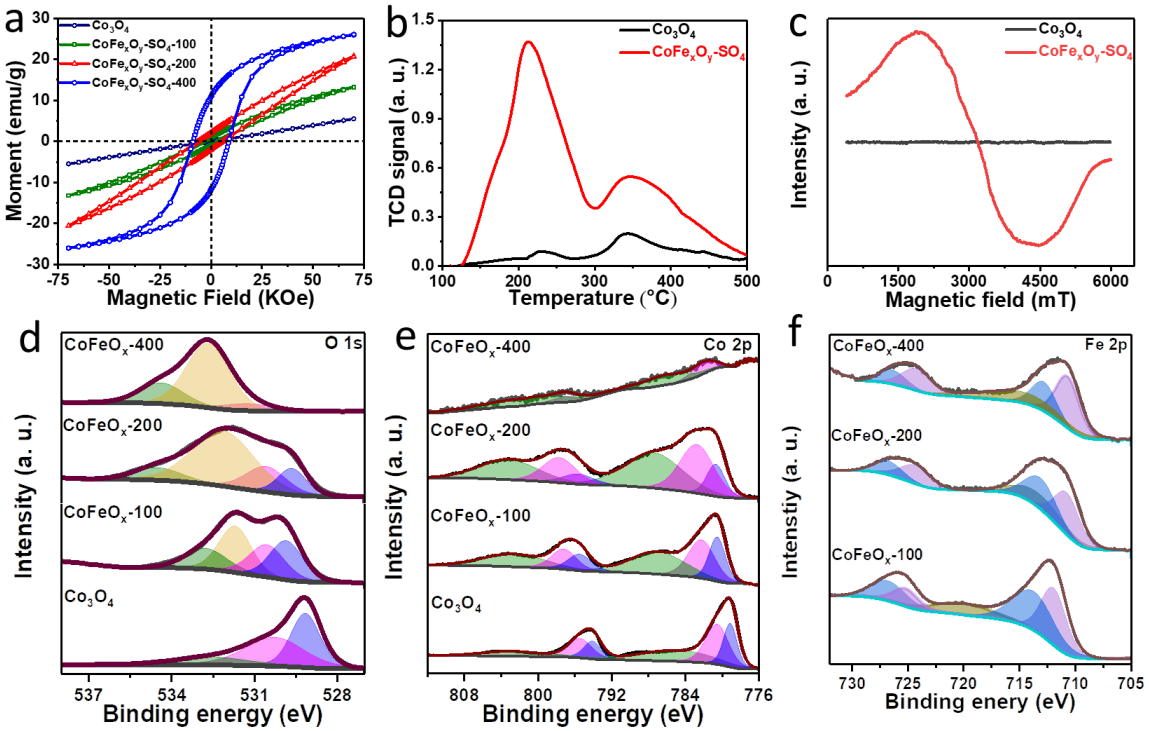

Figure 4 a) Magnetic hysteresis loops of $CoFe_xO_y$-100, 200, 400 and Co_3O_4 samples measured at 5 K. b - c) NH_3-TPD profiles EPR spectra of $CoFe_xO_y$-SO_4-200 and Co_3O_4. d-e) O 1s, Co 2p and Fe $2p_{3/2}$ XPS fitting of $CoFe_xO_y$-100, 200, 400 and Co_3O_4 samples.

The OER activity was initially assessed using linear sweep voltammetry (LSV) in a three-electrode set-up using a 1 M KOH electrolyte. A commercial IrO_2 electrocatalyst was analyzed as a reference. As shown in Figure 5a, at 10 mA cm^{-2}, Co_3O_4 exhibits a large overpotential of 339 mV indicating poor OER activity. After sulfate modification, the overpotential of Co_3O_4-SO_4 decreased to 325 mV at 10 mA cm^{-2}. By additionally incorporating iron, the OER activity strongly improved and the overpotential decreased down to 266 mV at 10 mA cm^{-2} for $CoFe_xO_y$-SO_4-200, well below that of the IrO_2 electrode (301 mV). This result demonstrates the important role played by Fe in the OER. However, when large amounts of Fe were introduced, a negative effect on the OER performance was observed, as shown for the $CoFe_xO_y$-SO_4-400 sample that was characterized by a large overpotential (361 mV). This result demonstrates that

Co also plays an important role in the OER, and thus an optimum Co/Fe ratio exists. Besides, the sulfate-free sample containing Co and Fe, $CoFe_xO_y$-Cl, also displayed a very poor OER performance, demonstrating the important role played by sulfate ions. In addition, an increase in the annealing temperature also resulted in a strong decrease in catalytic activity, which is related to the collapse of the porous structure and the crystallization of the material (Figure S17).

As shown in Figure 5b, $CoFe_xO_y$-SO_4-200 exhibited the best reaction kinetics with the smallest Tafel slope (46.5 mV dec^{-1}) among all catalysts tested, including the commercial IrO_2. Moreover, $CoFe_xO_y$-SO_4-200 also exhibits superior OER activity and kinetics than most previously reported oxide OER electrocatalysts (Figure 5d, Table S5).

The electrochemical active surface area (ECSA) was obtained from the double-layer capacitance (C_{dl}) determined by cyclic voltammetry (CV) at different scanning rates (Figure S18).[28, 55] C_{dl} was estimated from the linear fit of the charge current versus the scan rate (Figure 5d, Table S3). Considering a specific capacity of 0.04 mF cm^{-2},[56] ECSA was estimated at 224 cm^2 for $CoFe_xO_y$-SO_4-200, well above that of the other catalysts evaluated (Table S3). Figure 5e displays the ECSA-normalized specific activity. Despite its much larger ECSA, $CoFe_xO_y$-SO_4-200 also displayed the highest specific activity.[57] This high activity is related to a combination of different parameters, including a proper Co/Fe ratio, the presence of sulfate ions, the amorphous structure of the material, and its highly porous nanosheet-based geometry.

The Faradaic efficiency (FE) of the best-performing catalyst, $CoFe_xO_y$-SO_4-200A, was estimated using a rotating ring-disk electrode (RRDE). The disk current was set to 200 µA and the potential at the ring to 0.40 V vs. RHE. In these conditions, the oxygen generated at the disk electrode was reduced at the ring, where 39.1 µA current was measured (Figure 5f).[19] Considering an efficiency of collection of 0.2, a FE of 97.8 %, was determined, confirming that the measured oxidation current on $CoFe_xO_y$-SO_4 was provided from the OER.

Figure 5g displays the Nyquist plots of the EIS spectra measured with the different electrocatalysts. The measured semi-circles result from the rough surface structure of the electrodes and were accounted for by introducing a constant phase element (Q) simulating a

double-layer capacitor (C_{dl}). Since the OER involves at least two electrochemical processes, the formation of intermediates and subsequently O_2, an equivalent circuit with two RQ elements in series was considered to fit the EIS plots. We associate Q_1Rct_1 with the formation of intermediates and Q_2R_{ct2} with the oxygen evolution. Besides, R_s accounts mainly for the electrolyte resistance.[58, 59] Table S4 lists the parameters used for the EIS fitting. The smallest R_{ct} values obtained for $CoFe_xO_y$-SO_4-200 indicate the faster charge-transfer process taking place in this catalyst.

Figure 5h shows the LSV curves of the $CoFe_xO_y$-SO_4-200 after successive CV tests. The overpotential needed to catalyze water oxidation at 10 mA cm^{-2} was virtually the same before and after 2000 cycles test. Moreover, the chronoamperometry (i-t) and chronopotentiometry (E-t) durability test for $CoFe_xO_y$-SO_4-200 at the overpotential of 266 mV and 10 mA cm^{-2}, respectively, showed no obvious activity decay during 60 h of continuous test (Figure 5i), indicating that the $CoFe_xO_y$-SO_4-200 catalysts have excellent stability under the electrochemical conditions of water oxidation.

We analyzed the element content of Co, Fe, S within the electrolyte using ICP-MS during the OER chronoamperometry process (Figure S17c). The result showed that during the test just a minor amount of Co was lost. In contrast, the Fe content in the solution increased rapidly at first, then decreased slowly, and finally reached a dynamic stable equilibrium. As noted before, this dynamic Fe active site helps enhance OER activity.[60] Besides, a significant increase in the sulfur concentration was detected within the electrolyte during the first 3 h of reaction. The appearance of sulfur is due to the leaching of adsorbed sulfate ions during catalyst reconstitution. But XPS analysis showed part of the sulfate to be still present on the material surface after OER (Figure S16). It should be also noticed that the sulfate leaching did not affect the solution pH due to its small amount compared with the electrolyte volume.

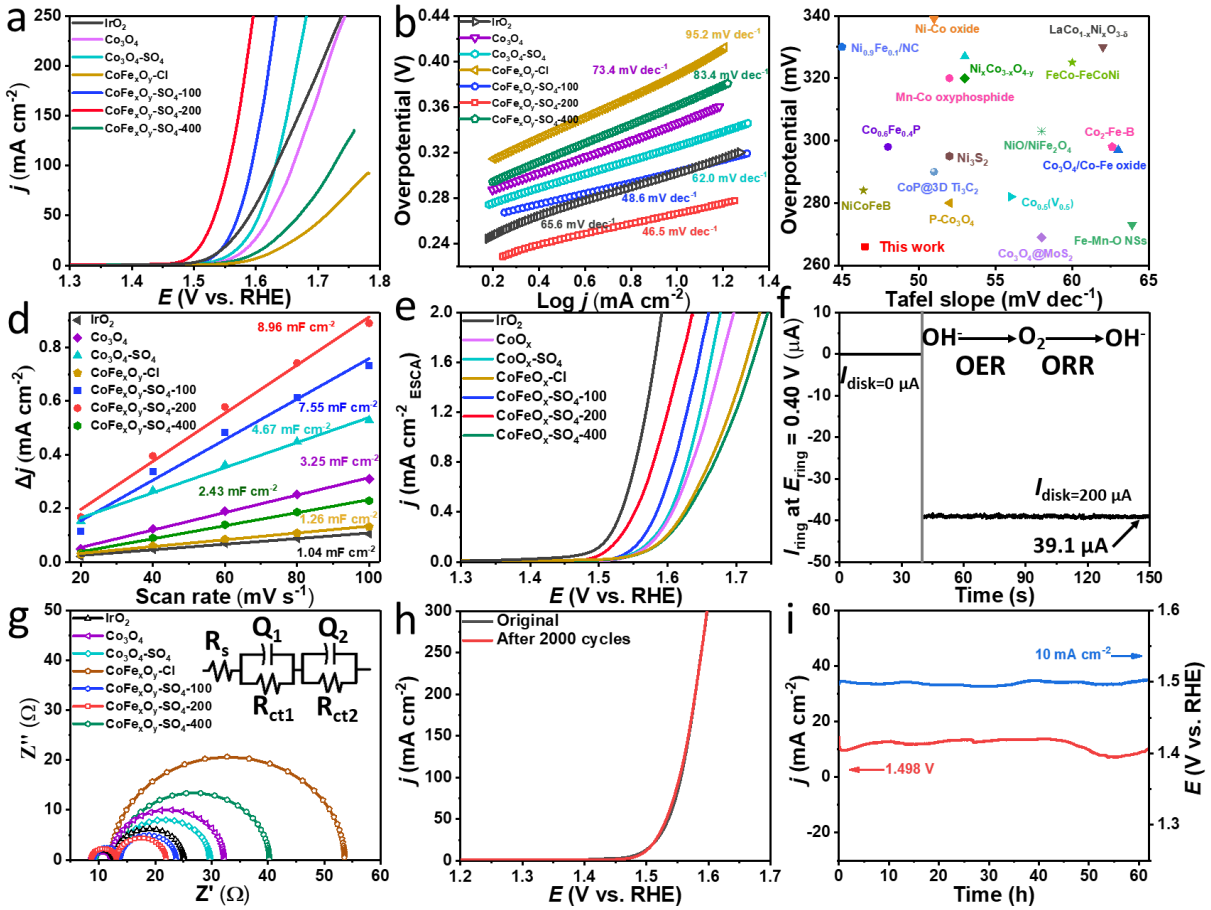

Figure 5. OER performance. a) LSV curves. b) Tafel plots. c) Overpotentials at 10 mA cm^{-2} and Tafel slopes of $CoFe_xO_y$-SO_4-200 and several previously reported cobalt electrocatalysts (Table S5). d) Capacitive current density at 1.17 V vs. RHE as a function of scan rate. e) ECSA-normalized OER polarization curves. f) Ring current of $CoFe_xO_y$-SO_4-200 on an RRDE (1500 rpm) in 1 M KOH solution (ring potential was set at 0.40 V vs. RHE). g) Nyquist plots at the potential of 1.52 V vs. RHE. h) LSV curves of $CoFe_xO_y$-SO_4-200 before and after 2000 cycles. i) Chronoamperometry at 1.50 V vs. RHE and chronopotentiometry at 10 mA cm^{-2} curve of $CoFe_xO_y$-SO_4-200.

To gain additional inside into the reaction kinetics of $CoFe_xO_y$-SO_4-200 catalyst and its evolution, in-situ Raman spectroscopy spectra were collected after CV cycles (1.3 to 1.7 V at 0.1 V s^{-1}) under a 1.0 M KOH electrolyte (Figures 6a and S19). After 200 CV cycles, a new broad peak at 550-600 cm^{-1} was detected and it was associated with the Co-O A_{1g} and E_g modes within CoOOH.[54, 59] Increasing the number of cycles, the peak intensity increased, which is correlated with an increase of the oxyhydroxide phase and points towards the conversion of the mixed-metal oxide surface to an oxyhydroxide. A band at 1000-1200 cm^{-1}, with a maximum at 1090 cm^{-1} and associated with superoxidic species ($CoOO^-$)[61], was also intensified upon cycling,

which demonstrates the creation and accumulation of such species with the OER. In contrast, there are no shifts in the Raman band positions or the appearance of new features during the entire test, just some decreases in the intensities of Raman peaks were observed with increasing CVs, owing to the formation of bubbles (Figure S20).[62] The comparison results further demonstrate that iron and sulfate ions play an important role in activating surface reconstruction, promoting oxygen-oxygen coupling, and improving OER performance, which is probably related to the stronger Lewis acid property of Fe^{3+} and SO_4^{2-} ions that makes them more likely to bond with OH^-.[12]

XPS analysis of the material after OER shows a shift of the Co 2p XPS spectrum to higher BEs, with its peaks becoming slightly narrower (Figure 6d). This result points toward the material oxidation from a Co^{2+} and Co^{3+} mixture to Co^{3+}, consistently with the surface conversion to metal oxyhydroxide observed by in situ Raman measurements.[19] Besides, the rest of the XPS spectra, and particularly the Fe 2p and O 1s regions, also slightly shift to lower BEs after the OER test (Figure 6e,f), which points towards an upward band bending at the material surface associated with a surface charge depletion, or a bulk-related downward shift of the Fermi level related to an increase of the hole concentration.

The adsorbate evolution mechanism (AEM, Figure 6b) drives OER in most catalysts, requiring surface sites able to properly bind the product species, intermediates, and reactants, i.e. not too strong and not too weak.[63, 64] However, as recently demonstrated, particularly active OER oxide catalysts enable their lattice oxygen to participate in the OER process (Figure 6c).[65-68] In such lattice oxygen oxidation mechanism (LOM), OER takes place through direct O-O binding, bypassing the adsorption of intermediates that limits AEM, thus resulting in higher OER activities. The LOM steps in a metal oxyhydroxide (MOOH) are schematized in Figure 6c.[69, 70 71] The LOM does not fully rely on the binding strength between involved species and surface sites, but also on the strength of the oxygen-metal bonds within the metal oxyhydroxide and the related bulk electronic properties, which can be adjusted by tuning the structure and composition of the catalyst. The variable valence of some transition metals, such as cobalt and iron, facilitates LOM. Under basic conditions, during OER, transition metal ions are easily oxidized to higher valence states, which act as catalytic active sites. Besides, the amorphous

structure of the material not only provides a higher density of undercoordinated atoms that enhance the adsorption of hydroxyl groups but also facilitates the change of oxidation state and promotes the participation of lattice oxygen in the OER.

In the LOM, the rate-limiting step is the deprotonation of hydroxyl groups. Thus the LOM-OER kinetics strongly depends on the electrolyte pH.[72, 73] On the other hand, the AEM-OER activity is limited by four concerted proton-electron transfer steps on surface metal centers, yielding a pH-independent performance. As displayed in Figure 6g,h, in contrast with the results obtained from Co_3O_4, the onset potential of $CoFe_xO_y$-SO_4 strongly decreases with increasing pH, pointing toward non-concerted proton transfer steps within LOM as the rate-limiting steps in the OER on this sample.

LOM is also distinguished from AEM by the direct O-O coupling that overcomes the limiting intermediate adsorption in AEM. Therefore, tracking the formation of peroxo-like (O_2^{2-}) and superoxo-like (O_2^-) species is another strategy to differentiate AEM and LOM. We used tetramethylammonium cations (TMA^+), which specifically bind with negatively charged oxygen molecules thus hampering LOM, to track the presence of these species within the electrolyte (1 M KOH + 1 M TMAOH).[19, 74] When introducing TMA^+ ions, we observed a notable reduction of the $CoFe_xO_y$-SO_4 OER activity, probing the fundamental role of LOM in the OER on this catalyst (Figure 6i). On the other hand, Co_3O_4 showed just a minor change in OER performance in the presence of 1 M TMAOH. Overall, these results suggest the high OER activity of OER $CoFe_xO_y$-SO_4 to be associated with the key role played by the LOM.

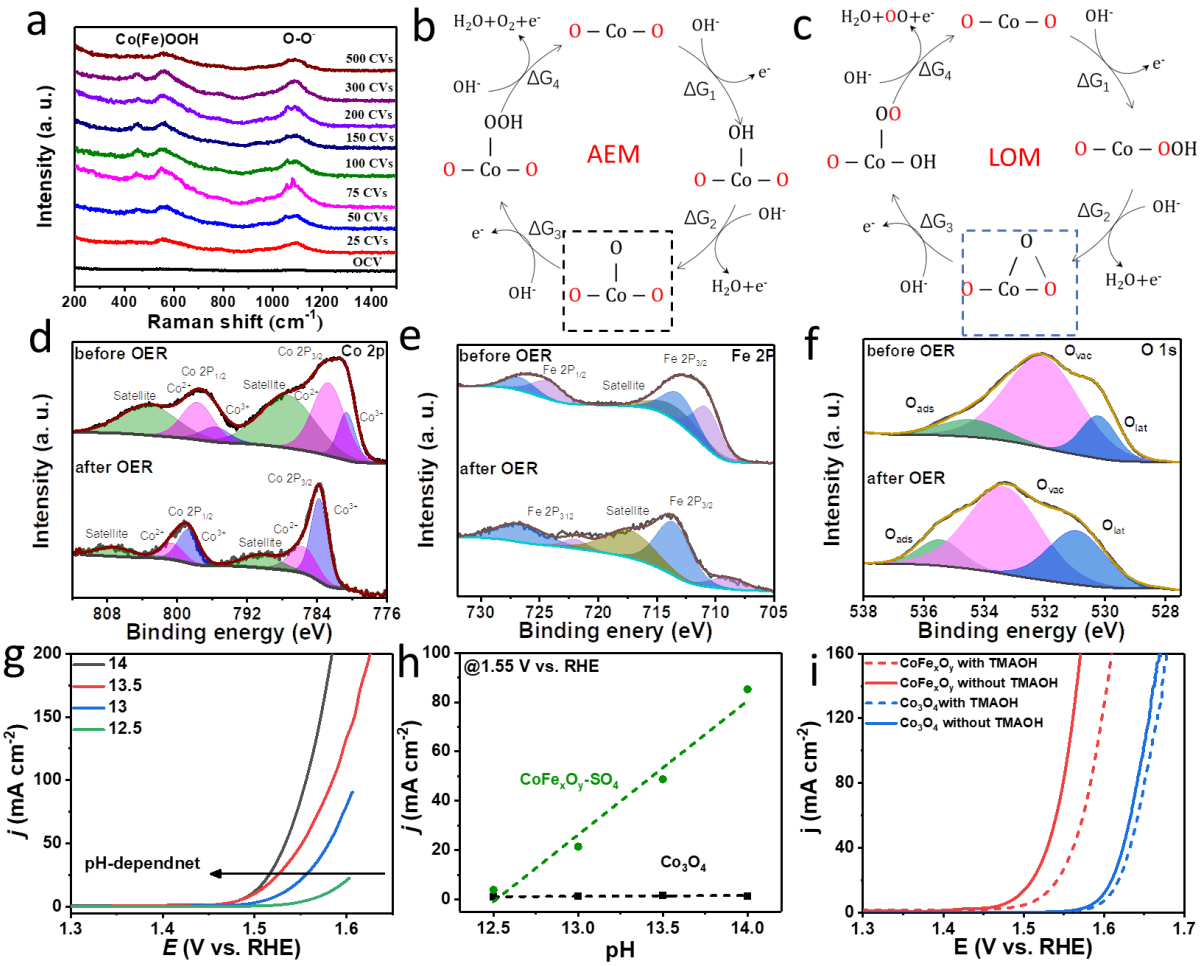

Figure 6. a) *In situ* Raman spectra of $CoFe_xO_y$-SO_4-200 after several CV cycles in 1.0 M KOH electrolyte. b-c) Scheme of the AEM and LOM OER processes, where □ represents an oxygen vacancy. d-f) High-resolution O 1s, Co 2p and Fe $2p_{3/2}$ XPS spectra of $CoFe_xO_y$-SO_4-200 before and after OER process. g) OER polarization curves of $CoFe_xO_y$-SO_4-200 at different pH values. h) Current densities $CoFe_xO_y$-SO_4-200 and Co_3O_4 at 1.5 V vs. RHE as a function of pH. i) OER polarization of $CoFe_xO_y$-SO_4-200 and Co_3O_4 in 1 M KOH with and without TMAOH.

In addition to experimental investigations, we performed a series of density functional theory (DFT) calculations to gain a fundamental understanding of the correlation between oxygen vacancies in cobalt iron dioxide and OER performance. Considering only the four-electron (4e) reaction pathway shown in Eqs. (S1)-(S4), we first calculated the Gibbs free energy of each elementary step for the AEM mechanism of $CoFeO_2$ with a perfect surface, and the AEM and LOM mechanisms of $CoFeO_2$ with oxygen vacancies, respectively. The calculated adsorption structures are shown in Figures 7a and S21-22. According to the calculations for the Gibbs free energy, as shown in Figure 7b, the reaction of step II, from *O to *OH, is the rate-determining step for both $CoFeO_2$ with a perfect surface (2.03 eV) and $CoFeO_2$ with oxygen vacancies (1.71

eV) according to the AEM mechanism. The lower Gibbs free energy change (0.32 eV) of the latter is consistent with the $CoFeO_2$ with oxygen vacancies having a higher OER activity than the $CoFeO_2$ with a perfect surface. Furthermore, the reaction of step Ⅳ, from *OOH to O_2, becomes the rate-determining step for the $CoFeO_2$ with oxygen vacancies according to the LOM mechanism. In this case, the largest Gibbs free energy change is 0.09 eV smaller than that for AEM on the same $CoFeO_2$ with oxygen vacancies. Thus, the LOM mechanism requires a lower overpotential to drive the oxidation of water. Overall, our calculations show that the OER catalytic activity of $CoFeO_2$ can be significantly increased by introducing oxygen vacancies and that the LOM mechanism is more favorable, which is consistent with the experimental results.

Furthermore, we analyzed the electronic structure of $CoFeO_2$ without and with oxygen vacancies using the projected density of states (PDOS). As shown in Figure 7c, when oxygen vacancies are introduced into $CoFeO_2$, new electronic states appear near the Fermi level, leading to an increase in the electrical conductivity of $CoFeO_2$, which also benefits the electrocatalytic activity of the material.[75]

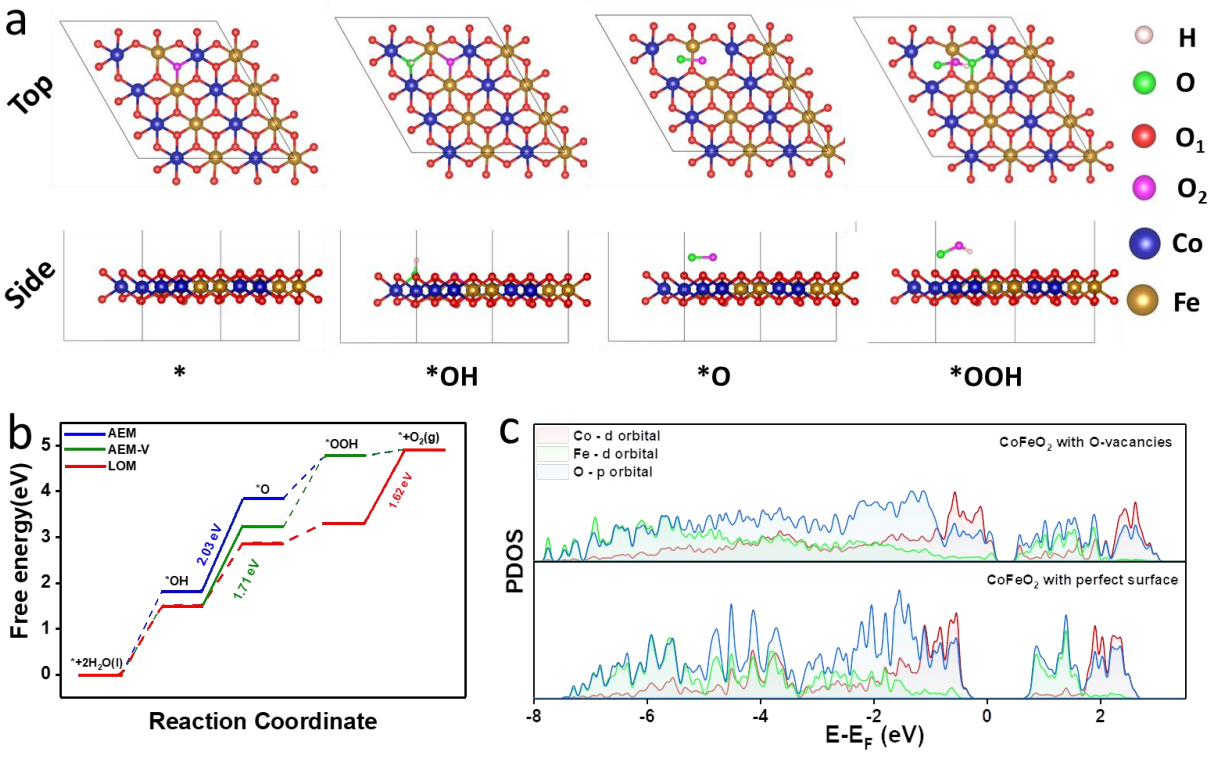

Figure 7. a) Top and side views of the optimized structures after adsorption of *OH, *O, and *OOH intermediates for the LOM on $CoFeO_2$ with oxygen vacancies (O_1 represents Lattice

oxygen, O_2 represent lattice oxygen in LOM). b) Free energies of OER steps in both mechanisms on $CoFeO_2$ with perfect surface and $CoFeO_2$ with oxygen vacancies. c) PDOS on $CoFeO_2$ with perfect surface and $CoFeO_2$ with oxygen vacancies.

After a long-term OER process, the catalyst was collected and analyzed. As shown in SEM and TEM images in Figures S23 and S24, the post-OER product maintained the ultrathin nanosheet structure with no obvious change. Moreover, both EDS elemental maps and HAADF-STEM images demonstrate the homogenous distribution of O, S, Co, and Fe to be preserved in the reacted material. (Figure S25)

3. Conclusion

In summary, cobalt-Iron oxide nanosheets containing SO_4^{2-} anionic groups were produced from the etching and partial cation exchange of a cobalt-based ZIF-67 with an ammonium iron sulfate. We show how this salt breaks the polyhedral structure of ZIF-67, yielding porous assemblies of nanosheets, containing controlled amounts of iron and sulfate ions. The material composition and crystal structure can be adjusted to optimize its OER performance. The optimized $CoFe_xO_y$-SO_4 sample displays an OER overpotential of 268 mV at 10 mA cm^{-2}, a Tafel slope of 46.5 mV dec^{-1}, and excellent stability during 62 h. We demonstrated this excellent performance to be associated with the presence of the three elements, cobalt, iron, and sulfate ions, and the porous and amorphous structure of the material. Raman spectroscopy analysis correlated with XPS data probes the material to be further oxidized to an oxohydroxide phase. It is further demonstrated here, that $CoFe_xO_y$-SO_4 samples catalyze the OER through an effective LOM mechanism.

4. Experimental section

4.1. Chemicals

Cobalt nitrate hexahydrate ($Co(NO_3)_2{\cdot}6H_2O$, 99.9%), ammonium iron(II) sulfate hexahydrate (Mohr's salt, $(NH_4)_2Fe(SO_4)_2{\cdot}6H_2O$, 99%), ammonium sulfate ($(NH_4)_2SO_4$, 99%), iron (II) chloride tetrahydrate ($FeCl_2{\cdot}6H_2O$, 99%), potassium hydroxide (KOH, 85%), and 2-methylimidazole ($C_4H_6N_2$, 99%) were purchased from Acros Organics. Iridium(IV) oxide (IrO_2, 99.9% metal basis) and Nafion (5 wt% in a mixture of low aliphatic alcohols and water) were obtained from Sigma-Aldrich. Methanol, ethanol, and isopropanol were of analytical grade and obtained from

various sources. Milli-Q water was obtained from a Purelab flex from Elga. All chemicals were used as received, without further purification.

4.2. Zeolitic imidazolate framework (ZIF-67)

ZIF-67 was obtained from a modified procedure based on previous reports[15, 37.] Briefly, 0.87 g $Co(NO_3)_2{\cdot}6H_2O$ was dissolved in 30 mL methanol. Subsequently, the clear solution obtained was poured into 30 mL methanol containing 1.97 g 2-methylimidazole under vigorous stirring. The obtained mixture was incubated for 24 h at room temperature. Purple precipitates were collected by centrifugation, washed with methanol at least three times, and finally dried at 60 °C overnight.

4.3. Synthesis of CoFe-MOFs.

120 mg of as-prepared ZIF-67 powder was ultrasonically re-dispersed in 20 mL ethanol. This dispersion was poured into 100 mL of an aqueous solution containing 100 mg, 200 mg or 400 mg $(NH_4)_2Fe(SO_4)_2{\cdot}6H_2O$ under continuous magnetic stirring. The mixture was then stirred vigorously for 12 hours at room temperature. Precipitates were collected by centrifugation, washed with water at least three times, and finally freeze-dried overnight. The obtained products were labeled as CoFe-MOFs-100, CoFe-MOFs-200, and CoFe-MOFs-400. To study the effect of the reaction time, CoFe-MOF-200 samples with different reaction times were also obtained by stirring ZIF-67 powder into a 100 mL aqueous solution containing 200 mg ammonium iron(II) sulfate for 1 hour or 3 hours. The effect of the Fe precursor and the SO_4^{2-} ions was studied by replacing $(NH4)_2Fe(SO_4)_2{\cdot}6H_2O$ with the same molar amount $FeCl_2$ or $(NH_4)_2SO_4$. These samples were labeled as $FeCl_2$-ZIF-67 and $(NH4)_2SO_4$-ZIF-67.

4.4. Synthesis of reference Co_3O_4 nanocrystals and amorphous $CoFe_xO_y$ nanosheets.

ZIF-67 and CoFe MOFs were annealed in a muffle furnace at 350 °C for 2 hours with a heating rate of 3 °C min^{-1} under air atmosphere. The black products obtained from the annealing of ZIF-67 and the different CoFe MOFs were denoted as Co_3O_4 and $CoFe_xO_y$-SO_4-100, $CoFe_xO_y$-SO_4-200, $CoFe_xO_y$-SO_4-400, $CoFe_xO_y$-Cl, and Co_3O_4-SO_4, respectively. The effect of the annealing temperature was studied by annealing the CoFe-MOFs-200 at 450 °C and 550 °C for 2 hours in air. The obtained samples were named $CoFe_xO_y$-SO_4-450℃ and $CoFe_xO_y$-SO_4-550℃,

respectively. Table S1 displays the complete list of samples produced and analyzed in this work.

ASSOCIATED CONTENT

Supporting Information

The Supporting Information is available free of charge at XXX

Materials, product analysis and computational methods, additional XRD, SEM, TEM/ STEM, HRETEM, EELS, pore size distribution, magnetization curves, XPS spectra, ICP-OES results, In situ Raman spectra, DFT data of control samples and catalysts, more electrocatalytic tests data (ECSA, impedance, and activity), and comparison tables of OER property.

Author Contributions

The manuscript was written through the contributions of all authors. All authors have approved the final version of the manuscript.

Notes

The authors declare no competing financial interest

ACKNOWLEDGEMENTS

The authors thank the support from the projects Combenergy (PID2019−105490RB−C32) from the Spanish Ministerio de Ciencia e Innovación, ENE2016-77798-C4-3-R and NANOGEN (PID2020-116093RB-C43), funded by MCIN/ AEI/10.13039/501100011033/ and by “ERDF A way of making Europe”, by the “European Union”. X. W., X. H., C. X., and R. D. thank the China Scholarship Council (CSC) for the scholarship support. The authors acknowledge funding from Generalitat de Catalunya 2017 SGR 327 and 2017 SGR 1246. ICN2 acknowledges the Severo Ochoa program from Spanish MINECO (Grant No. SEV-2017-0706). IREC and ICN2 are funded by the CERCA Programme /Generalitat de Catalunya. Z. L. acknowledges funding from MINECO SO-FPT PhD grant (SEV-2013-0295-17-1). J.L. is a Serra Húnter Fellow and is grateful to MICINN/FEDER RTI2018-093996-B-C31, GC 2017 SGR 128 and ICREA Academia program. Part of the present work has been performed in the frameworks of Universitat de Barcelona

Nanoscience PhD program and Universitat Autònoma de Barcelona Materials Science PhD program.

REFERENCES

1. Stamenkovic, V. R.; Strmcnik, D.; Lopes, P. P.; Markovic, N. M., Energy and fuels from electrochemical interfaces. *Nat. Mater.* **2016,** *16* (1), 57-69.
2. Sui, Y.; Ji, X., Anticatalytic Strategies to Suppress Water Electrolysis in Aqueous Batteries. *Chem. Rev.* **2021,** *121* (11), 6654-6695.
3. Wu, Z. P.; Lu, X. F.; Zang, S. Q.; Lou, X. W., Non-Noble-Metal-Based Electrocatalysts toward the Oxygen Evolution Reaction. *Adv. Funct. Mater.* **2020,** *30* (15), 1910274.
4. Song, J.; Wei, C.; Huang, Z. F.; Liu, C.; Zeng, L.; Wang, X.; Xu, Z. J., A review on fundamentals for designing oxygen evolution electrocatalysts. *Chem. Soc. Rev.* **2020,** *49* (7), 2196-2214.
5. Lu, Y.; Dong, C. L.; Huang, Y. C.; Zou, Y.; Liu, Z.; Liu, Y.; Li, Y.; He, N.; Shi, J.; Wang, S., Identifying the Geometric Site Dependence of Spinel Oxides for the Electrooxidation of 5-Hydroxymethylfurfural. *Angew. Chem., Int. Ed.* **2020,** *59* (43), 19215-19221.
6. Yu, M.; Budiyanto, E.; Tuysuz, H., Principles of Water Electrolysis and Recent Progress in Cobalt-, Nickel-, and Iron-Based Oxides for the Oxygen Evolution Reaction. *Angew. Chem., Int. Ed.* **2022,** *61*(1), e202103824.
7. Song, F.; Bai, L.; Moysiadou, A.; Lee, S.; Hu, C.; Liardet, L.; Hu, X., Transition Metal Oxides as Electrocatalysts for the Oxygen Evolution Reaction in Alkaline Solutions: An Application-Inspired Renaissance. *J. Am. Chem. Soc.* **2018,** *140* (25), 7748-7759.
8. Zhang, L.; Jang, H.; Liu, H.; Kim, M. G.; Yang, D.; Liu, S.; Liu, X.; Cho, J., Sodium-Decorated Amorphous/Crystalline RuO_2 with Rich Oxygen Vacancies: A Robust pH-Universal Oxygen Evolution Electrocatalyst. *Angew. Chem., Int. Ed.* **2021,** *60* (34), 18821-18829.
9. Zhang, G.; Li, Y.; Xiao, X.; Shan, Y.; Bai, Y.; Xue, H. G.; Pang, H.; Tian, Z.; Xu, Q., In Situ Anchoring Polymetallic Phosphide Nanoparticles within Porous Prussian Blue Analogue Nanocages for Boosting Oxygen Evolution Catalysis. *Nano Lett.* **2021,** *21* (7), 3016-3025.
10. Yin, J.; Jin, J.; Lin, H.; Yin, Z.; Li, J.; Lu, M.; Guo, L.; Xi, P.; Tang, Y.; Yan, C. H., Optimized Metal Chalcogenides for Boosting Water Splitting. *Adv. Sci.* **2020,** *7* (10), 1903070.
11. Jin, S., Are Metal Chalcogenides, Nitrides, and Phosphides Oxygen Evolution Catalysts or Bifunctional Catalysts? *ACS Energy Lett.* **2017,** *2* (8), 1937-1938.
12. Gao, L.; Cui, X.; Sewell, C. D.; Li, J.; Lin, Z., Recent advances in activating surface reconstruction for the high-efficiency oxygen evolution reaction. *Chem. Soc. Rev.* **2021,** *50* (15), 8428-8469.
13. Zuo, Y.; Liu, Y.; Li, J.; Du, R.; Han, X.; Zhang, T.; Arbiol, J.; Divins, N. J.; Llorca, J.; Guijarro, N., In situ electrochemical oxidation of Cu_2S into CuO nanowires as a durable and efficient electrocatalyst for oxygen evolution reaction. *Chem. Mater.* **2019,** *31* (18), 7732-7743.
14. Gao, L.; Cui, X.; Wang, Z.; Sewell, C. D.; Li, Z.; Liang, S.; Zhang, M.; Li, J.; Hu, Y.; Lin, Z., Operando unraveling photothermal-promoted dynamic active-sites generation in $NiFe_2O_4$ for markedly enhanced oxygen evolution. *Proc. Natl. Acad. Sci.* **2021,** *118* (7), e2023421118.
15. Shi, Z.; Yu, Z.; Jiang, R.; Huang, J.; Hou, Y.; Chen, J.; Zhang, Y.; Zhu, H.; Wang, B.; Pang, H., MOF-derived M-OOH with rich oxygen defects by in situ electro-oxidation reconstitution for a

highly efficient oxygen evolution reaction. *J. Mater. Chem. A.* **2021,** *9* (18), 11415-11426.
16. Wu, Z. P.; Zhang, H.; Zuo, S.; Wang, Y.; Zhang, S. L.; Zhang, J.; Zang, S. Q.; Lou, X. W., Manipulating the Local Coordination and Electronic Structures for Efficient Electrocatalytic Oxygen Evolution. *Adv. Mater.* **2021,** *33* (40), 2103004.
17. Cheng, W.; Xi, S.; Wu, Z.-P.; Luan, D.; Lou, X. W., In situ activation of Br-confined Ni-based metal-organic framework hollow prisms toward efficient electrochemical oxygen evolution. *Sci. Adv.* **2021,** *7* (46), eabk0919.
18. Zhang, J.-Y.; Yan, Y.; Mei, B.; Qi, R.; He, T.; Wang, Z.; Fang, W.; Zaman, S.; Su, Y.; Ding, S.; Xia, B. Y., Local spin-state tuning of cobalt–iron selenide nanoframes for the boosted oxygen evolution. *Energy Environ. Sci.* **2021,** *14* (1), 365-373.
19. Li, X.; Xiao, L.; Zhou, L.; Xu, Q.; Weng, J.; Xu, J.; Liu, B., Adaptive Bifunctional Electrocatalyst of Amorphous CoFe Oxide @ 2D Black Phosphorus for Overall Water Splitting. *Angew. Chem., Int. Ed.* **2020,** *59* (47), 21106-21113.
20. Fan, K.; Zou, H.; Lu, Y.; Chen, H.; Li, F.; Liu, J.; Sun, L.; Tong, L.; Toney, M. F.; Sui, M.; Yu, J., Direct Observation of Structural Evolution of Metal Chalcogenide in Electrocatalytic Water Oxidation. *ACS Nano* **2018,** *12* (12), 12369-12379.
21. Shi, Y.; Du, W.; Zhou, W.; Wang, C.; Lu, S.; Lu, S.; Zhang, B., Unveiling the Promotion of Surface-Adsorbed Chalcogenate on the Electrocatalytic Oxygen Evolution Reaction. *Angew. Chem., Int. Ed.* **2020,** *59* (50), 22470-22474.
22. Li, S.; Li, Z.; Ma, R.; Gao, C.; Liu, L.; Hu, L.; Zhu, J.; Sun, T.; Tang, Y.; Liu, D.; Wang, J., A Glass-Ceramic with Accelerated Surface Reconstruction toward the Efficient Oxygen Evolution Reaction. *Angew. Chem., Int. Ed.* **2021,** *60* (7), 3773-3780.
23. Liao, H.; Luo, T.; Tan, P.; Chen, K.; Lu, L.; Liu, Y.; Liu, M.; Pan, J., Unveiling Role of Sulfate Ion in Nickel-Iron (oxy)Hydroxide with Enhanced Oxygen-Evolving Performance. *Adv. Funct. Mater.* **2021**. 31(38): 2102772.
24. Xue, Y.; Fang, J.; Wang, X.; Xu, Z.; Zhang, Y.; Lv, Q.; Liu, M.; Zhu, W.; Zhuang, Z., Sulfate-Functionalized $RuFeO_x$ as Highly Efficient Oxygen Evolution Reaction Electrocatalyst in Acid. *Adv. Funct. Mater.* **2021,** 31 (32): 2101405.
25. Zhang, R.; Wang, L.; Pan, L.; Chen, Z.; Jia, W.; Zhang, X.; Zou, J.-J., Solid-acid-mediated electronic structure regulation of electrocatalysts and scaling relation breaking of oxygen evolution reaction. *Appl. Catal.* **2020,** 277, 119237
26. Qiao, C.; Usman, Z.; Cao, T.; Rafai, S.; Wang, Z.; Zhu, Y.; Cao, C.; Zhang, J., High-valence Ni and Fe sites on sulfated NiFe-LDH nanosheets to enhance O-O coupling for water oxidation. *Chem. Eng. J.* **2021,** 426, 130873.
27. Huang, W.; Zhang, J.; Liu, D.; Xu, W.; Wang, Y.; Yao, J.; Tan, H. T.; Dinh, K. N.; Wu, C.; Kuang, M.; Fang, W.; Dangol, R.; Song, L.; Zhou, K.; Liu, C.; Xu, J. W.; Liu, B.; Yan, Q., Tuning the Electronic Structures of Multimetal Oxide Nanoplates to Realize Favorable Adsorption Energies of Oxygenated Intermediates. *ACS Nano* **2020**, 14(12), 17640-17651.
28. Kwon, J.; Han, H.; Jo, S.; Choi, S.; Chung, K. Y.; Ali, G.; Park, K.; Paik, U.; Song, T., Amorphous Nickel–Iron Borophosphate for a Robust and Efficient Oxygen Evolution Reaction. *Adv. Energy Mater.* **2021**, 11(25): 2100624.
29. Indra, A.; Menezes, P. W.; Sahraie, N. R.; Bergmann, A.; Das, C.; Tallarida, M.; Schmeisser, D.; Strasser, P.; Driess, M., Unification of catalytic water oxidation and oxygen reduction reactions: amorphous beat crystalline cobalt iron oxides. *J. Am. Chem. Soc.* **2014,** *136* (50),

17530-6.
30. Liu, J.; Ji, Y.; Nai, J.; Niu, X.; Luo, Y.; Guo, L.; Yang, S., Ultrathin amorphous cobalt–vanadium hydr(oxy)oxide catalysts for the oxygen evolution reaction. *Energy Environ. Sci.* **2018,** *11* (7), 1736-1741.
31. Li, S.; Yang, X.; Yang, S.; Gao, Q.; Zhang, S.; Yu, X.; Fang, Y.; Yang, S.; Cai, X., An amorphous trimetallic (Ni–Co–Fe) hydroxide-sheathed 3D bifunctional electrode for superior oxygen evolution and high-performance cable-type flexible zinc–air batteries. *J. Mater. Chem. A* **2020,** *8* (11), 5601-5611.
32. Chen, G.; Zhu, Y.; Chen, H. M.; Hu, Z.; Hung, S. F.; Ma, N.; Dai, J.; Lin, H. J.; Chen, C. T.; Zhou, W.; Shao, Z., An Amorphous Nickel-Iron-Based Electrocatalyst with Unusual Local Structures for Ultrafast Oxygen Evolution Reaction. *Adv. Mater.,* **2019,** *31* (28), e1900883.
33. Anantharaj, S.; Noda, S., Amorphous Catalysts and Electrochemical Water Splitting: An Untold Story of Harmony. *Small* **2020,** *16* (2), e1905779.
34. Liu, W.; Liu, H.; Dang, L.; Zhang, H.; Wu, X.; Yang, B.; Li, Z.; Zhang, X.; Lei, L.; Jin, S., Amorphous Cobalt-Iron Hydroxide Nanosheet Electrocatalyst for Efficient Electrochemical and Photo-Electrochemical Oxygen Evolution. *Adv. Funct. Mater.* **2017,** *27* (14).
35. Chen, H.; Chen, J.; Ning, P.; Chen, X.; Liang, J.; Yao, X.; Chen, D.; Qin, L.; Huang, Y.; Wen, Z., 2D Heterostructure of Amorphous CoFeB Coating Black Phosphorus Nanosheets with Optimal Oxygen Intermediate Absorption for Improved Electrocatalytic Water Oxidation. *ACS Nano* **2021**, 15(7), 12418-12428.
36. Cai, W.; Chen, R.; Yang, H.; Tao, H. B.; Wang, H. Y.; Gao, J.; Liu, W.; Liu, S.; Hung, S. F.; Liu, B., Amorphous versus Crystalline in Water Oxidation Catalysis: A Case Study of NiFe Alloy. *Nano Lett.,* **2020,** 20(6), 4278-4285.
37. Kuang, M.; Zhang, J.; Liu, D.; Tan, H.; Dinh, K. N.; Yang, L.; Ren, H.; Huang, W.; Fang, W.; Yao, J.; Hao, X.; Xu, J.; Liu, C.; Song, L.; Liu, B.; Yan, Q., Amorphous/Crystalline Heterostructured Cobalt-Vanadium-Iron (Oxy)hydroxides for Highly Efficient Oxygen Evolution Reaction. *Adv. Energy Mater.* **2020,** *10* (43): 2002215.
38. Xu, H.; Fei, B.; Cai, G.; Ha, Y.; Liu, J.; Jia, H.; Zhang, J.; Liu, M.; Wu, R., Boronization-Induced Ultrathin 2D Nanosheets with Abundant Crystalline–Amorphous Phase Boundary Supported on Nickel Foam toward Efficient Water Splitting. *Adv. Energy Mater.* **2019,** *10* (3): 1902714.
39. Yang, N.; Cheng, H.; Liu, X.; Yun, Q.; Chen, Y.; Li, B.; Chen, B.; Zhang, Z.; Chen, X.; Lu, Q.; Huang, J.; Huang, Y.; Zong, Y.; Yang, Y.; Gu, L.; Zhang, H., Amorphous/Crystalline Hetero-Phase Pd Nanosheets: One-Pot Synthesis and Highly Selective Hydrogenation Reaction. *Adv. Mater.* **2018,** 30 (39), e1803234.
40. Wang, X.; Huang, X.; Gao, W.; Tang, Y.; Jiang, P.; Lan, K.; Yang, R.; Wang, B.; Li, R., Metal–organic framework derived $CoTe_2$ encapsulated in nitrogen-doped carbon nanotube frameworks: a high-efficiency bifunctional electrocatalyst for overall water splitting. *J. Mater. Chem. A* **2018,** *6* (8), 3684-3691.
41. Wang, X.; Li, F.; Li, W.; Gao, W.; Tang, Y.; Li, R., Hollow bimetallic cobalt-based selenide polyhedrons derived from metal–organic framework: an efficient bifunctional electrocatalyst for overall water splitting. *J. Mater. Chem. A* **2017,** *5* (34), 17982-17989.
42. Huang, Y.; Zhang, S. L.; Lu, X. F.; Wu, Z. P.; Luan, D.; Lou, X. W., Trimetallic Spinel $NiCo_{2-x}FexO_4$ Nanoboxes for Highly Efficient Electrocatalytic Oxygen Evolution. *Angew. Chem., Int. Ed.* **2021,** *60* (21), 11841-11846.

43. Yu, X.; Yu, Z.-Y.; Zhang, X.-L.; Li, P.; Sun, B.; Gao, X.; Yan, K.; Liu, H.; Duan, Y.; Gao, M.-R.; Wang, G.; Yu, S.-H., Highly disordered cobalt oxide nanostructure induced by sulfur incorporation for efficient overall water splitting. *Nano Energy* **2020,** *71*: 104652.
44. Li, G.; Zhang, X.; Zhang, H.; Liao, C.; Jiang, G., Bottom-up MOF-intermediated synthesis of 3D hierarchical flower-like cobalt-based homobimetallic phophide composed of ultrathin nanosheets for highly efficient oxygen evolution reaction. *Appl. Catal., B* **2019,** *249*, 147-154.
45. Wang, C.; Chen, W.; Yuan, D.; Qian, S.; Cai, D.; Jiang, J.; Zhang, S., Tailoring the nanostructure and electronic configuration of metal phosphides for efficient electrocatalytic oxygen evolution reactions. *Nano Energy* **2020,** 69, 104453.
46. Zhang, Y.; Liang, C.; Wu, J.; Liu, H.; Zhang, B.; Jiang, Z.; Li, S.; Xu, P., Recent Advances in Magnetic Field-Enhanced Electrocatalysis. *ACS Appl. Energy Mater.* **2020,** *3* (11), 10303-10316.
47. Yao, J.; Huang, W.; Fang, W.; Kuang, M.; Jia, N.; Ren, H.; Liu, D.; Lv, C.; Liu, C.; Xu, J.; Yan, Q., Promoting Electrocatalytic Hydrogen Evolution Reaction and Oxygen Evolution Reaction by Fields: Effects of Electric Field, Magnetic Field, Strain, and Light. *Small Methods* **2020,** *4* (10): 2000494.
48. Wang, Q.; Xue, X.; Lei, Y.; Wang, Y.; Feng, Y.; Xiong, X.; Wang, D.; Li, Y., Engineering of Electronic States on Co_3O_4 Ultrathin Nanosheets by Cation Substitution and Anion Vacancies for Oxygen Evolution Reaction. *Small* **2020,** *16* (24), e2001571.
49. Duan, Y.; Yu, Z. Y.; Hu, S. J.; Zheng, X. S.; Zhang, C. T.; Ding, H. H.; Hu, B. C.; Fu, Q. Q.; Yu, Z. L.; Zheng, X., Scaled-up synthesis of amorphous NiFeMo oxides and their rapid surface reconstruction for superior oxygen evolution catalysis. *Angew. Chem., Int. Ed* **2019,** *58* (44), 15772-15777.
50. Xu, W.; Gao, W.; Meng, L.; Tian, W.; Li, L., Incorporation of Sulfate Anions and Sulfur Vacancies in $ZnIn_2S_4$ Photoanode for Enhanced Photoelectrochemical Water Splitting. *Advanced Energy Materials* **2021,** *11* (26).
51. Qiu, B.; Wang, C.; Zhang, N.; Cai, L.; Xiong, Y.; Chai, Y., CeO2-Induced Interfacial Co^{2+} Octahedral Sites and Oxygen Vacancies for Water Oxidation. *ACS Catal.* **2019,** *9* (7), 6484-6490.
52. Zhuang, L.; Ge, L.; Yang, Y.; Li, M.; Jia, Y.; Yao, X.; Zhu, Z., Ultrathin Iron-Cobalt Oxide Nanosheets with Abundant Oxygen Vacancies for the Oxygen Evolution Reaction. *Adv. Mater.* **2017,** *29* (17): 1606793.
53. Xiao, Z.; Wang, Y.; Huang, Y.-C.; Wei, Z.; Dong, C.-L.; Ma, J.; Shen, S.; Li, Y.; Wang, S., Filling the oxygen vacancies in Co_3O_4 with phosphorus: an ultra-efficient electrocatalyst for overall water splitting. *Energy Environ. Sci.* **2017,** *10* (12), 2563-2569.
54. Qian, Q.; Li, Y.; Liu, Y.; Zhang, G., General anion-exchange reaction derived amorphous mixed-metal oxides hollow nanoprisms for highly efficient water oxidation electrocatalysis. *Appl. Catal., B* **2020,** *266*, 118642
55. Wu, G.; Zheng, X.; Cui, P.; Jiang, H.; Wang, X.; Qu, Y.; Chen, W.; Lin, Y.; Li, H.; Han, X.; Hu, Y.; Liu, P.; Zhang, Q.; Ge, J.; Yao, Y.; Sun, R.; Wu, Y.; Gu, L.; Hong, X.; Li, Y., A general synthesis approach for amorphous noble metal nanosheets. *Nat. Commun.* **2019,** *10* (1), 4855.
56. Yang, X.; Sun, X.; Gan, L.-Y.; Sun, L.; Mi, H.; Zhang, P.; Ren, X.; Li, Y., A CoO_x/FeO_x heterojunction on carbon nanotubes prepared by plasma-enhanced atomic layer deposition for the highly efficient electrocatalysis of oxygen evolution reactions. *J. Mater. Chem. A* **2020,** 8 (30), 15140-15147.
57. Zhang, S. L.; Guan, B. Y.; Lu, X. F.; Xi, S.; Du, Y.; Lou, X. W., Metal Atom-Doped Co_3O_4

Hierarchical Nanoplates for Electrocatalytic Oxygen Evolution. *Adv. Mater.* **2020,** 32 (31), 2002235.
58. Bo, X.; Hocking, R. K.; Zhou, S.; Li, Y.; Chen, X.; Zhuang, J.; Du, Y.; Zhao, C., Capturing the active sites of multimetallic (oxy)hydroxides for the oxygen evolution reaction. *Energy Environ. Sci.* **2020,** *13* (11), 4225-4237.
59. Bo, X.; Li, Y.; Chen, X.; Zhao, C., Operando Raman Spectroscopy Reveals Cr-Induced-Phase Reconstruction of NiFe and CoFe Oxyhydroxides for Enhanced Electrocatalytic Water Oxidation. *Chem. Mater.* **2020,** 32 (10), 4303-4311.
60. Chung, D. Y.; Lopes, P. P.; Farinazzo Bergamo Dias Martins, P.; He, H.; Kawaguchi, T.; Zapol, P.; You, H.; Tripkovic, D.; Strmcnik, D.; Zhu, Y. J. N. E., Dynamic stability of active sites in hydr (oxy) oxides for the oxygen evolution reaction. *Nat. Energy* **2020,** 5 (3), 222-230.
61. Moysiadou, A.; Lee, S.; Hsu, C. S.; Chen, H. M.; Hu, X., Mechanism of Oxygen Evolution Catalyzed by Cobalt Oxyhydroxide: Cobalt Superoxide Species as a Key Intermediate and Dioxygen Release as a Rate-Determining Step. *J. Am. Chem. Soc.* **2020,** 142 (27), 11901-11914.
62. Solomon, G.; Landström, A.; Mazzaro, R.; Jugovac, M.; Moras, P.; Cattaruzza, E.; Morandi, V.; Concina, I.; Vomiero, A., $NiMoO_4$@Co_3O_4 Core–Shell Nanorods: In Situ Catalyst Reconstruction toward High Efficiency Oxygen Evolution Reaction. *Adv. Energy Mater.* **2021,** 11 (32): 2101324
63. Ooka, H.; Huang, J.; Exner, K. S., The Sabatier Principle in Electrocatalysis: Basics, Limitations, and Extensions. *Front. Energy Res.* **2021,** *9*, 155.
64. Sabatier, P., La Catalyse En Chimie Organique; Encyclopédie de science chimique appliquée. *Ch Béranger* **1913**.
65. Pan, Y.; Xu, X.; Zhong, Y.; Ge, L.; Chen, Y.; Veder, J. M.; Guan, D.; O'Hayre, R.; Li, M.; Wang, G.; Wang, H.; Zhou, W.; Shao, Z., Direct evidence of boosted oxygen evolution over perovskite by enhanced lattice oxygen participation. *Nat. Commun.* **2020,** *11* (1), 2002.
66. Yoo, J. S.; Rong, X.; Liu, Y.; Kolpak, A. M., Role of Lattice Oxygen Participation in Understanding Trends in the Oxygen Evolution Reaction on Perovskites. *ACS Catal.* **2018,** *8* (5), 4628-4636.
67. Liu, Y.; Luo, X.; Zhou, C.; Du, S.; Zhen, D.; Chen, B.; Li, J.; Wu, Q.; Iru, Y.; Chen, D., A modulated electronic state strategy designed to integrate active HER and OER components as hybrid heterostructures for efficient overall water splitting. *Appl. Catal. B* **2020,** 260, 118197.
68. Xu, S.; Lv, C.; He, T.; Huang, Z.; Zhang, C., Amorphous film of cerium doped cobalt oxide as a highly efficient electrocatalyst for oxygen evolution reaction. *J. Mater. Chem. A* **2019,** *7* (13), 7526-7532.
69. Duan, Y.; Sun, S.; Sun, Y.; Xi, S.; Chi, X.; Zhang, Q.; Ren, X.; Wang, J.; Ong, S. J. H.; Du, Y., Mastering surface reconstruction of metastable spinel oxides for better water oxidation. *Adv. mater.* **2019,** 31 (12), 1807898.
70. Zhu, Y.; Tahini, H. A.; Hu, Z.; Chen, Z. G.; Zhou, W.; Komarek, A. C.; Lin, Q.; Lin, H. J.; Chen, C. T.; Zhong, Y.; Fernandez-Diaz, M. T.; Smith, S. C.; Wang, H.; Liu, M.; Shao, Z., Boosting Oxygen Evolution Reaction by Creating Both Metal Ion and Lattice-Oxygen Active Sites in a Complex Oxide. *Adv. Mater.* **2020,** 32 (1), e1905025.
71. Grimaud, A.; Diaz-Morales, O.; Han, B.; Hong, W. T.; Lee, Y. L.; Giordano, L.; Stoerzinger, K. A.; Koper, M. T. M.; Shao-Horn, Y., Activating lattice oxygen redox reactions in metal oxides to catalyse oxygen evolution. *Nat. Chem.* **2017,** 9 (5), 457-465.

72. Zhang, P.; Li, L.; Nordlund, D.; Chen, H.; Fan, L.; Zhang, B.; Sheng, X.; Daniel, Q.; Sun, L., Dendritic core-shell nickel-iron-copper metal/metal oxide electrode for efficient electrocatalytic water oxidation. *Nat. Commun.* **2018,** 9 (1), 381.
73. Grimaud, A.; Hong, W.; Shao-Horn, Y.; Tarascon, J., Anionic Redox Processes for Enhanced Battery and Water Splitting Devices. *Nat. Mater.* **2016,** 15 (2), 121-126.
74. Huang, Z.-F.; Song, J.; Du, Y.; Xi, S.; Dou, S.; Nsanzimana, J. M. V.; Wang, C.; Xu, Z. J.; Wang, X., Chemical and structural origin of lattice oxygen oxidation in Co–Zn oxyhydroxide oxygen evolution electrocatalysts. *Nat. Energy* **2019,** 4 (4), 329-338.
75. Wang, Y.; Zhang, Y.; Liu, Z.; Xie, C.; Feng, S.; Liu, D.; Shao, M.; Wang, S. J. A. C. I. E., Layered double hydroxide nanosheets with multiple vacancies obtained by dry exfoliation as highly efficient oxygen evolution electrocatalysts. *Angew. Chem., Int. Ed.* **2017,** *56* (21), 5867-5871.

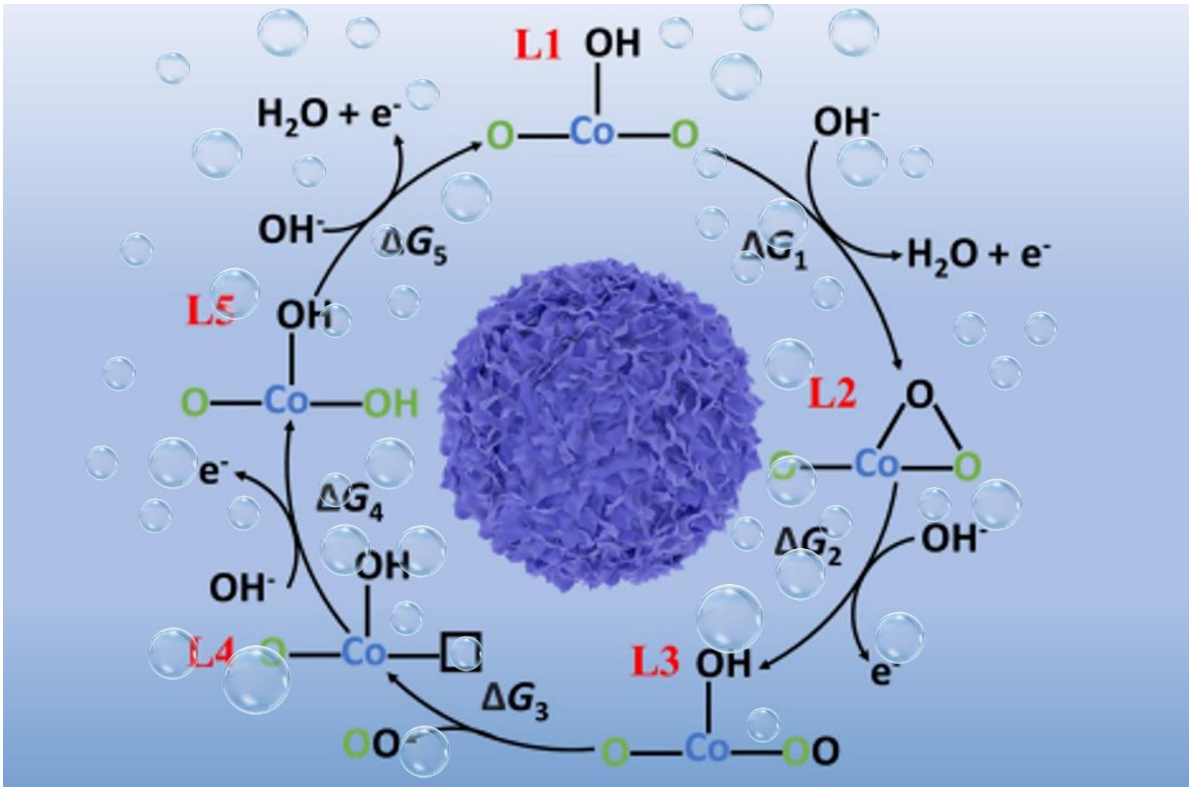
L1
OH
O—Co—O
H2O + e-
OH-
ΔG5
ΔG1
OH-
H2O + e-
L5
OH
O—Co—OH
L2
O
O—Co—O
e-
ΔG4
ΔG2
OH-
OH-
OH
L4
O—Co—□
L3
OH
ΔG3
OO
O—Co—OO
e-

TOC Graphic